Carbohydrate Polymer Technologies and Applications 3 (2022) 100193

Contents lists available at ScienceDirect

Carbohydrate Polymer Technologies and Applications

journal homepage: www.sciencedirect.com/journal/carbohydrate-polymer-technologies-and-applications

Controlling the structure and properties of semi-crystalline cellulose/silk-fibroin biocomposites by ionic liquid type and hydrogen peroxide concentration

Stacy A. Love [a], Xiao Hu [b], David Salas-de la Cruz [a,c,*]

[a] The Center for Computational and Integrative Biology, Rutgers University, Camden, NJ United States
[b] Department of Physics & Astronomy, Department of Biomedical Engineering, Rowan University, Glassboro, NJ United States
[c] Department of Chemistry, Rutgers University, Camden, NJ United States

ARTICLE INFO

Keywords:
Cellulose II
Semi-crystallinity
β-sheet
Imidazolium
Hydrogen peroxide

ABSTRACT

This work reports how to tune the semi-crystallinity of a blended microcrystalline cellulose/silk-fibroin biocomposite using ionic liquids and various coagulation agents. The morphological and thermal properties of a blended 1:1 polymeric system are studied as a function of polymer fabrication parameters. Ionic liquids, 1-ethyl-3-methylimidazolium acetate verses 1-ethyl-3-methylimidazolium chloride, are used as competing solvent types and six hydrogen peroxide solutions (1—25%) plus water are used as varying coagulation agents. Analysis of the results demonstrate that solvent anion type, Ac^- verses Cl^-, affects protein secondary structure formation, and that solvent anion type and the concentration of hydrogen peroxide changes morphology and thermal stability of the regenerated materials. Polymers dissolved in 1-ethyl-3-methylimidazolium acetate are less thermally stable than those dissolved in 1-ethyl-3-methylimidazolium chloride. Furthermore, carbohydrate microcrystal size is positively correlated to hydrogen peroxide concentration upon fabrication and is calculated to have either a gradual or step transition increase in microcrystal size depending upon the solvent's anion type.

1. Introduction

Cellulose is commonly studied in materials research because of its desirable structural properties, renewability, biodegradability, and biological inertness. Cellulose is derived from many natural resources, e.g., wood and cotton, and therefore is a widely abundant and inexpensive biopolymer available for research. However, cellulose has unique dissolution properties and there exists a capability of transitioning cellulose I (natural cellulose) into polymorphs II and III (regenerated forms of cellulose) (French & Cintrón, 2013 Isogai & Atalla, 1998; Stanton et al., 2018;). These assorted cellulose polymorphs correspond to different hydrogen-bond locations between oxygens within their lattice structures. Upon comparing cellulose I to its polymorph counterparts, types II and III, natural cellulose (type I) is arranged in a parallel form, is more crystalline, and contains a higher elastic modulus (Nishino, Takano & Nakamae, 1995 Šturcová, Davies & Eichhorn, 2005;). However, it is hypothesized that the anti-parallel arrangements of types II and III are thermally favorable when compared to the parallel arrangement of cellulose I (Yue, 2011). Furthermore, regeneration processes can cause cellulose I to shift to type II, whereas other treatments, e.g., liquid NH_3 or diamine treatment, will cause a shift from type I to type III. Cellulose III can transition back to types II or I through treatment with hot water or by heating (Kovalenko, 2010 Wada, 2001;). Cellulose may also be blended with other macromolecules to promote even greater changes to the material's properties. In fact, cellulose's versatility in chemical polymorphism permits it to act as a compelling and robust choice for research in polymer blends. Microcrystalline cellulose (MCC) is one of the most utilized derivatives of cellulose (A. F. Tarchoun, Trache, Klapötke & Khimeche, 2020). It is a commercially available nanostructure material and is produced through an acid hydrolysis process to remove amorphous regions within the cellulose structure (A. F. Tarchoun et al., 2020). Classified mainly as refined wood pulp, the structure of MCC exists as cellulose I. MCC also contains a large amount of active hydroxyl groups along its surface chain backbone, thus, making it capable of inserting different functional groups for specific mechanical and thermo properties (A. F. Tarchoun et al., 2020). However, once MCC is blended with other polymers, some of its crystalline features are lost from the process of dissolution and regeneration.

---

* Corresponding author.
E-mail address: ds1191@camden.rutgers.edu (D. Salas-de la Cruz).

https://doi.org/10.1016/j.carpta.2022.100193
Received 23 November 2021; Received in revised form 31 January 2022; Accepted 12 February 2022

Therefore, more research is needed in how to enhance or decrease specific material properties such as semi-crystallinity by altering the chemicals used to regenerate blended polymer systems.

Like MCC and other cellulose derivatives, silk is a desirable material in research because it adds diverse and flexible material properties to a blended polymer system. Silk-fibroin (SF) is the major protein in silk, and it contains a repetitive hexapeptide sequence of Gly-Ser-Gly-Ala-Gly-Ala. The high glycine content of this sequence allows for tight packing of stable antiparallel β-sheet crystallites, which effectively contributes to this protein's high tensile strength. SF is useful for many applications such as biomedicine, sensor technology, and textile manufacturing. There are two main crystal structures within SF, silk I and silk II. A third unstable antiparallel β-sheet structure, silk III, may be seen at the air to water interface in regenerated SF (Qi et al., 2017). The metastable structure of silk I contains a crank or zigzag spatial conformation, whereas silk II belongs to the monoclinic system and forms an antiparallel β-sheet structure. Alcohol or potassium phosphate treatments can easily convert the structures of silk I into silk II (Qi et al., 2017 Valluzzi, Gido, Muller & Kaplan, 1999;). Furthermore, a change in flexibility and tensile strength is seen for polymer composites when carbohydrates like cellulose are blended with fibrous SF strands (Yao et al., 2015).

Biocomposites such as cellulose and SF are processed by dissolution followed by a regenerative phase known as coagulation. Both steps provide a pathway to tune the materials' physicochemical and morphological properties (Bealer et al., 2020 Blessing et al., 2019;, 2020 Gough, Rivera-Galletti, Cowan, Salas-De La Cruz & Hu, 2020; Hadadi et al., 2018; Oldenkamp, Vela Ramirez & Peppas, 2019;). In such fabrication methods, solvents and coagulants are essential as they are the driving forces behind the solubility and thus the morphology of regenerated macromolecules. A poor solvent will significantly affect the miscibility of the polymers and will affect certain physicochemical properties of the blend (Isogai & Atalla, 1998 Wang, Chen, Yang & Shao, 2013;). Imidazolium-based ionic liquids (ILs) are molten salts consisting of a large organic cation and a smaller inorganic anion. ILs can be used as a viable solvent for organic compounds (DeFrates et al., 2017 Phillips et al., 2004; Stanton et al., 2018;) and research on ILs is booming due to their chemical and thermal stability, non-flammability, reusability, and versatile dissolution capabilities. Furthermore, ILs are diverse in their ionic combinations (Benedetto, Ballone & Engineering, 2016 Marsh, Boxall & Lichtenthaler, 2004;). The number of possible binary types is on the order of at least 10^6, allowing for many different parameters to suit the unique dissolution properties of large organic compounds. This is important because many biological macromolecules contain relatively strong intermolecular forces that hold their three-dimensional structures close together. ILs can not only break these strong intermolecular forces but depending upon the macromolecule's primary structure, the macromolecule's molecular weight may also remain intact. Research incorporating ILs as solvents for MCC and SF has broadened the applicational scope for regenerated natural materials (Zhu et al., 2006). For example, ILs can help incorporate functional additives to MCC and other biological materials, e.g., dyes, complexants, and other polymers (Miller et al., 2021 Zhu et al., 2006;). In particular, ILs with imidazolium bases are more stable than other nitrogen-containing heterocycles such as pyridinium, triazolium, tetrazolium, or piperidinium (Achour et al., 2021). However, the thermal stability of imidazolium-based ILs coupled with halides such as $Br^-$and $Cl^-$is lower compared to other ion types due to their nucleophilic abilities (Achour et al., 2021 Noorhisham et al., 2021;). The use of ILs as green solvents will also decrease the dependency on non-renewable petroleum-based synthetic solvents typically needed for larger organic macromolecules. Therefore, more studies on IL anion type would be particularly useful to environmentally-conscious applications.

Depending upon which chemical agent is used for coagulation, different physical and chemical properties of the blended system will be induced and can be further fine-tuned by using different concentrations of the coagulant (Blessing et al., 2020 Love, Popov, Rybacki, Hu & Salas-de la Cruz, 2020;). Within our research, hydrogen peroxide (H_2O_2) solutions are used to diffuse IL salts from the polymer matrix as well as regenerate the composites. We have reported in previous work that greater H_2O_2 concentrations are positively correlated to greater cellulose II microcrystal sizes within the polymer blends. This means that we can tune up or down the microcrystal size, i.e., semi-crystallinity, of cellulose II within a cellulose-silk (CELL-SF) blend through the regenerative process alone. This study is an extension of that work, providing further insights into the physicochemical differences between regenerated blended biopolymers by comparing two different imidazolium-based ILs as the polymer solvent. Taking into consideration that ILs can successfully disrupt the hydrogen-bonds between biopolymer chains, the proposed theory is that different anions (Ac^- vs. Cl^-) in an imidazolium-based IL will produce a different amount of "empty" volume between polymer chains upon dissolution. With the understanding that nucleophilic capabilities differ between these two ion types, this volume change will affect molecular interactions within the matrix. After dissolution, molecules of H_2O_2 and water will disperse into the polymer-solvent matrix while simultaneously diffusing out the solvent molecules to regenerate a solid film. Therefore, our hypothesis states that this combined process of solvent diffusion and polymer regeneration during biocomposite fabrication will produce different morphologies as functions of solvent anion type, coagulant concentration, or both. Here, we fabricated and compared two sample-sets of 1:1 CELL-SF blends. One set was produced by the solvent, 1-ethyl-3-methyl imidazolium acetate ($[EMIM]^+[Ac]^-$) and the other by 1-ethyl-3-methyl imidazolium chloride ($[EMIM]^+[Cl]^-$); both sets contained multiple samples that were regenerated in water and six increasing concentrations of H_2O_2 solution (1%, 2%, 5%, 10%, 15%, and 25% vol. in H_2O). This generated a total of seven different samples per set. The morphology and thermal properties of the blends were analyzed as a function of fabrication parameters, i.e., solvent anion type and concentration of the H_2O_2 coagulant. Characterization tests used for this investigation were Fourier Transform Infrared Spectroscopy (FTIR), Thermal Gravimetric Analysis (TGA), and X-ray Scattering (XRS).

2. Materials and methods

2.1. Materials

Avicel microcrystalline cellulose (Techware: Z26578–0) was acquired from Analtech. Prior to use, the cellulose powder was placed in a vacuum oven at 50 °C for 24 h (Liu et al., 2011). Silk cocoons of Bombyx mori mulberry silkworms were obtained from Treenway Silks (Lakewood, CO). To remove the sericin coating on the silk fibers, silkworm cocoons were boiled in a 0.02 M $NaHCO_3$ (CAS-No. 497–19–8 Sigma-Aldrich, USA) solution for 15 min and then rinsed thoroughly with deionized water three times for complete removal. The degummed silk fibroin was air dried overnight and then placed into a vacuum oven to remove any surface moisture. The ionic liquids, 1-ethyl-3-methylimidazolium acetate (CAS-No. 143,314–17–4) and 1-ethyl-3-methylimidazolium chloride (CAS-No. 65,039–09–0), were purchased from Sigma-Aldrich and were pretreated before use. IL pretreatment consisted of placing the solvent in a vacuum oven set to 30 inHg and 50 °C for 24 h to ensure that all water molecules were removed (Blessing et al., 2019 Hadadi et al., 2018;). ACS reagent-grade (Quality Level 200) H_2O_2 solution at 30 wt.% in H_2O with inhibitor (CAS-No. 7722–84–1) was purchased from Sigma-Aldrich. All H_2O_2 solutions were diluted to the desired concentrations prior to use.

2.2. Fabrication method

For the fabrication of blended samples, the polymer composition was 10% of the solution's total weight, while the IL consisted of the remaining 90%. The ratio of polymers was 1:1 Avicel microcrystalline cellulose to mori silk-fibroin. The IL was heated on a hot plate at 85 °C, and mori silk-fibroin was added first to the solvent. After silk dissolution, microcrystalline Avicel cellulose powder was slowly added and then left to agitate on the hotplate for 24 h. The newly blended solution was transferred into 3D-printed mold kits of dimensions 12 mm x 12 mm x 1 mm. Each mold kit containing the solvent-polymer mixture was then placed in 100 mL of the coagulation agent, distilled water or various concentrations of H_2O_2 solution. Immersion in the coagulation solution effects the removal of IL from the samples, as well as regeneration of the blended polymers. The beakers containing the coagulant and solvent-polymer blend were then sealed with Parafilm and left for 48 h at RT. After this coagulation phase, the mold kits containing the polymer blend were removed from their solutions and placed in a Teflon evaporating plate. This entire system was transferred to a vacuum oven set to 30 inHg and 50 °C for 24 h (Hadadi et al., 2018 Love et al., 2020; Stanton et al., 2018;). The samples were removed from their mold kits and sealed in a desiccator for long term storage. Refer to Schematic 1 for a visualization of this three-step fabrication process.

2.3. Structural characterization method

The structural study of the samples was conducted using a Bruker's ALPHA-Platinum Attenuated Total Reflectance Fourier Transform Infrared (ATR-FTIR) Spectrometer with a platinum-diamond sample module. A spectrum between 4000 cm^{-1}–400 cm^{-1} was performed per each scan at a resolution of 4 cm^{-1}. 128 background scans were completed along with 32 sample scans at 6 different sample locations. The mean result of 6 different locations was chosen for analysis, and a min-max normalization was applied to all spectra. IR analyses were performed using Opus 7.2 software. Fourier self-deconvolution was applied to each spectrum to study the protein's amide I and II regions (1595–1705 cm^{-1}). The purpose of this technique was to calculate protein secondary structure content. The Lorentzian line shape, with a 25.614 cm^{-1} half-bandwidth and a noise reduction factor of 0.3, was used for performing peak deconvolution. All secondary structure regions were assigned a specific wavenumber range adapted from Hu et al. and a Gaussian function was utilized for each fitted peak under the spectrum. Refer to S1 in the supplementary data for a visualization of this technique. Secondary structure percent was calculated from the integrals of the fitted peaks (Hu, Kaplan & Cebe, 2006). If we label all integrals I_n for $n \in N = \{1, \ldots m\}$ where m is the total number of integrals, let J contain the set of integrals of an individual secondary structure. Then if S is the percent of that secondary structure, S is given by:

$$S = \sum_{j \in J} I_j \Big/ \sum_{n \in N} I_n$$

These fitting functions and calculations were repeated 4 x to calculate the standard error from the mean. For visualization purposes, the full spectra plots were normalized using min-max normalization.

2.4. Thermal characterization method

Thermogravimetric analysis (TGA) was performed using TA Instruments Discovery TGA system on 5 mg samples. All samples went under a nitrogen gas purge of 25 mL/min at 30 °C. The procedure consisted of an isothermal period of one minute, followed by a thermal rate of 10 °C/min up to 600 °C. Step transition analyses and derivative plots were conducted to determine the temperature onset of decomposition (TOnset), the maximum end temperature of degradation (TEnd), the weight-loss percentage of the sample, and the value which corresponds to the decomposition of the sample at the highest rate of change with respect to temperature (TΔMax).

2.5. Morphological characterization method

The morphological studies were conducted using a Dual Environmental X-ray Scattering System (XRS) at the University of Pennsylvania under vacuum. The Xeuss 2.0 by XENOCS has a Cu x-ray source, computer controlled focusing and transmission incident sample geometries, a 1 M pixel Pilatus detector (2D), and a smaller detector for simultaneous small-angle scattering (SAXS) and wide-angle scattering (WAXS) acquisition. Only WAXS data are reported for this study. A full-flux collimation was used with a slit size of 1.2 mm × 1.2 mm. Each sample-run was executed for a total of 300 s. The intensity reported is not absolute intensity and, thus, is in arbitrary units (a.u.). All samples were taped to a sample-holder and placed under vacuum for data acquisition. The XRS profiles were evaluated using Foxtrot 3.4.9; the isotropic 2D scattering patterns were azimuthally integrated to yield intensity versus scattering vector (q). Azimuthal integration was used for all XRS plots and graphed at $2\theta°$. Three different methods for determining the full width at half-maximum (FWHM) using the software, OriginPro 2019, were performed and the mean crystal size was obtained for comparison purposes relative to this study. Crystal size calculations were conducted using unnormalized raw data via the Scherrer equation:

$$\tau = \frac{K\lambda}{\beta cos\theta}$$

Where τ is the mean size of the crystal; K is the dimensionless shape factor (0.94); λ is the wavelength of the incident x-ray beam (0.54 nm); β represents the full width at half-maximum (FWHM) of the scattering peak in radians, and θ is the Bragg angle. Cellulose surface chains within the microcrystal occupy an approximate layer thickness of 0.57 nm, adapted from RH Newman, and so the proportion of crystallite interior chains was calculated using the equation:

$$\chi = \frac{(\tau - 2h)^2}{\tau^2}$$

Here χ is the proportion of crystallite interior chains; τ is the crystallite size calculated from the Scherrer equation, and h is the layer thickness of the chain (~0.57 nm). The values of χ were used as estimates of the fraction of cellulose chains enclosed in the interior of the crystallites (Newman, 1999 Poletto, Zattera, Forte & Santana, 2012;).

3. Results and discussion

3.1. Structural analysis

Fourier Transform Infrared Spectroscopy (FTIR) was used to verify proper polymer regeneration Fig. 1. shows prominent IR absorbance bands in all spectra for both sets at 3600–3000 cm^{-1}, 3000–2750 cm^{-1}, and 1180–930 cm^{-1} for Cellulose –OH, –CH, and –CO stretching modes, respectively. SF's amide I (1720–1600 cm^{-1}) and amide II (1590–1500 cm^{-1}) regions are also present, and absorbance bands at all aforementioned regions verify adequate regeneration of CELL-SF within the blends. The amide I region of SF was used to calculate its secondary structure content, e.g., turns, side chains, β-sheets, and random coils and α-helices combined. The fitting parameters used to calculate the protein secondary structure content were established by Hu, Xiao et al. (Hu et al., 2006) and Fig. 2 shows the amide I region after Fourier deconvolution. Wavenumber ranges for different protein secondary structures are shown schematically as different colored regions under the curve. Refer to Fig. 3 for all calculated values.

Shifting of the peaks can be seen when comparing our spectra to an FTIR amide I spectrum of pure SF. Refer to S3 in the supplementary data for a pure SF spectrogram. Therefore, multiple curve-fitting trials were performed and a standard error from the mean was calculated. The results are interpreted such that very subtle percent changes were calculated in SF secondary structure content as they relate to H_2O_2

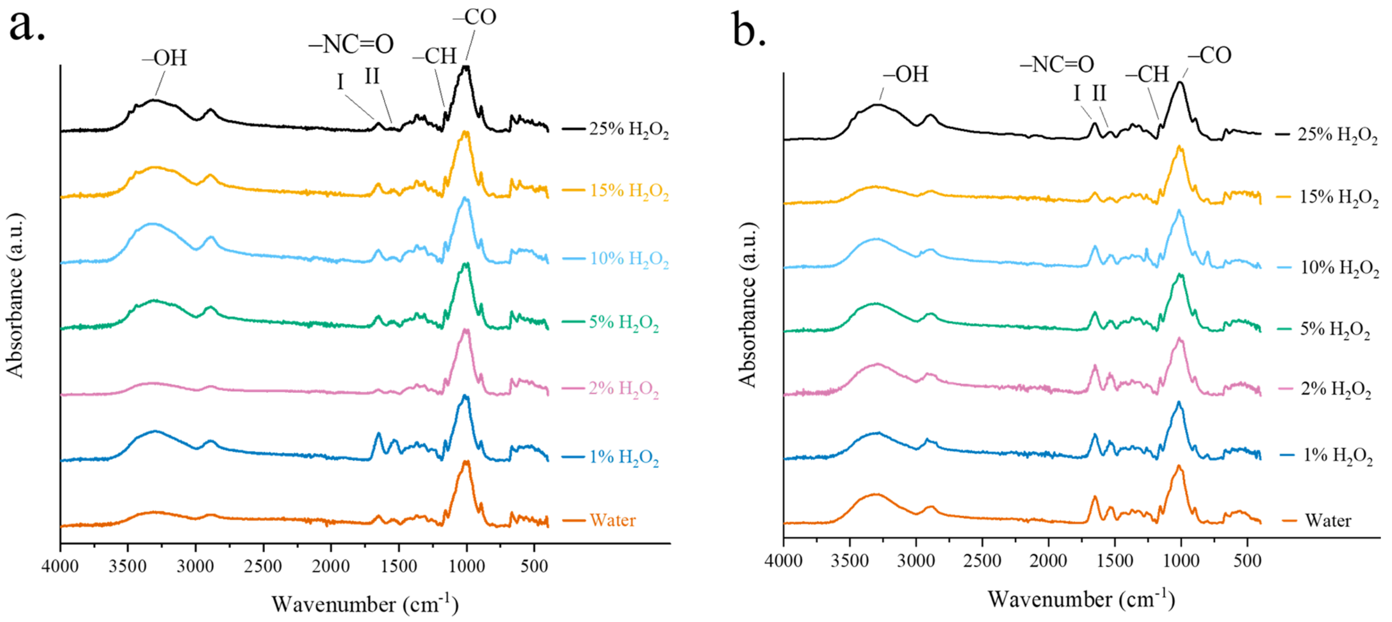

Fig. 1. Normalized FTIR data for regenerated 1:1 CELL-SF composition samples dissolved in IL solvents (a.) [EMIM]$^+$[Ac]$^-$ and (b.) [EMIM]$^+$[C*l*]$^-$. Samples are differentiated based on the coagulation agents used during regeneration, water and different H_2O_2 solutions (listed on legend). Prominent IR absorbance bands are labelled at 3600–3000 cm^{-1}, 3000–2750 cm^{-1}, and 1180–930 cm^{-1} for CELL –OH, –CH, and –CO stretching modes, respectively. SF's amide I (1720–1600 cm^{-1}) and amide II (1590–1500 cm^{-1}) regions are also labelled in both spectrograms.

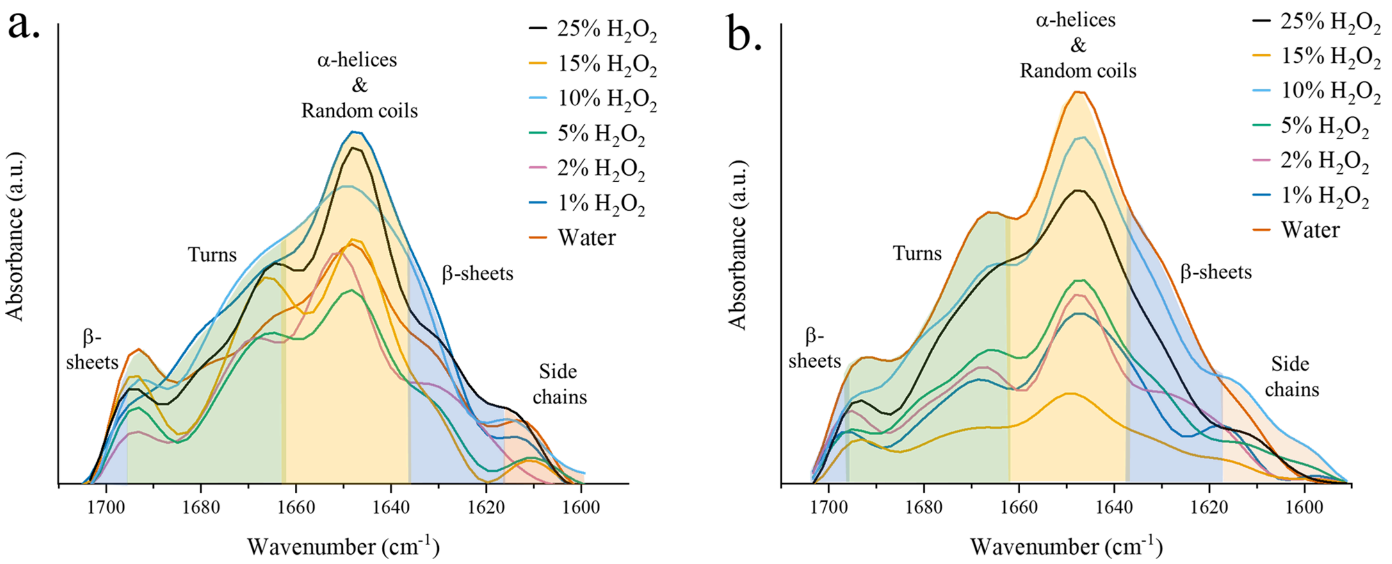

Fig. 2. FTIR SF amide I region data (not normalized) after Fourier deconvolution for regenerated 1:1 CELL-SF composition samples. Plots show samples dissolved in one of two different IL solvents, (a.) [EMIM]$^+$[Ac]$^-$ and (b.) [EMIM]$^+$[C*l*]$^-$. Samples are differentiated based on the coagulation agents used during regeneration, water and different H_2O_2 solutions (listed on legend).

concentration used during the fabrication process. In other words, no true patten exists when evaluating for changes to protein structure by coagulant concentration within either set. This finding correlates well to previously published work that investigated a different polymer ratio of 9:1 CELL-SF biocomposites dissolved in an imidazolium-based IL and coagulated in similar H_2O_2 solutions (Love et al., 2020) Fig. 3. shows more overall amorphous secondary structures verses crystalline structures were calculated for all samples within both sets. However, upon closer analysis of the data, some trends do occur when examining between sets. In other words, there are different percentages calculated for samples coagulated in identical H_2O_2 solutions but dissolved in different ILs. In fact, the protein secondary structure content changes as a function of the solvent anion type used during polymer dissolution. β-sheet content increases slightly as a function of the IL's anion, Cl$^-$, and four out of the seven samples (samples coagulated in 2%, 5%, 10%, and 15% vol. H_2O_2 in H_2O) show statistical significance for this claim. When we examine the amorphous structures of the protein, it was calculated that the opposite is true for random coils and α-helices. Here, if we continue the comparison between sets, more random coil and α-helix conformations were calculated for the samples dissolved in [EMIM][Ac$^-$] and coagulated in identical H_2O_2 concentrations. However, it must be noted that only the 2% H_2O_2-coagulated sample has statistical significance to this claim, and that two additional samples (samples coagulated in 10% and 25% vol. H_2O_2 in H_2O) show minor statistical significance. Lastly, if we compare the percentages of turns calculated within the amide I region between both sets, a greater number of turns were calculated for

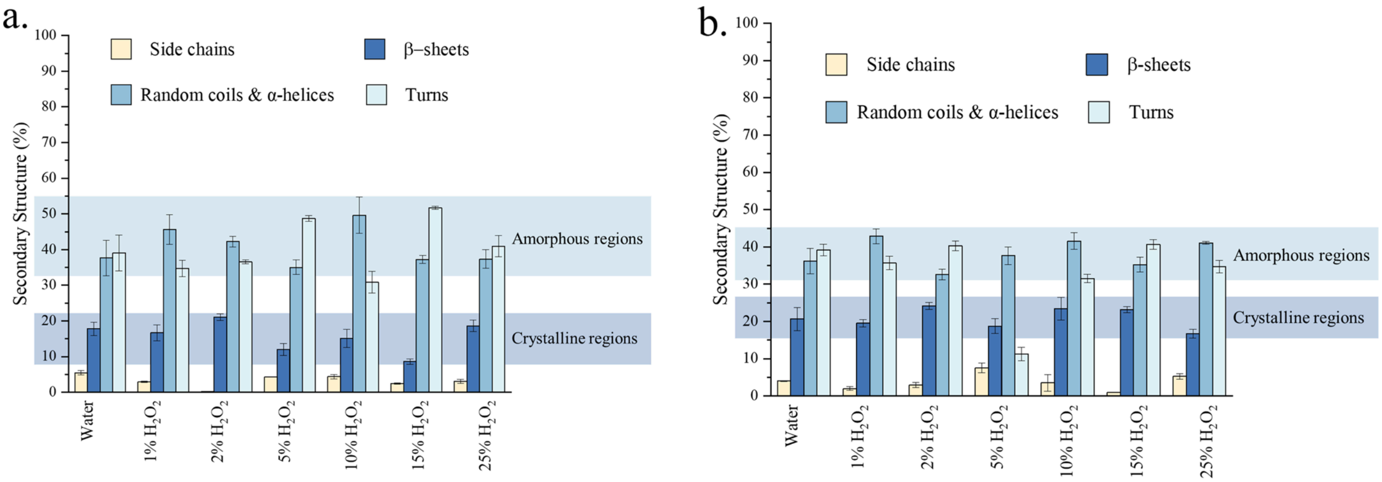

Fig. 3. Secondary Structure Percentages calculated from the integrals of the fitted peaks performed after Fourier deconvolution on the amide I region of SF (refer to Fig. 2). Regenerated 1:1 CELL-SF composition samples dissolved in IL solvents (a.) $[EMIM]^+[Ac]^-$ and (b.) $[EMIM]^+[Cl]^-$. Samples are differentiated based on the coagulation agents used during regeneration, water and different H_2O_2 solutions (listed on x-axis). Each secondary structures' standard error from the mean is shown on the graph ($n = 4$). The SF amorphous (light blue) and crystalline (dark blue) regions represent the full range of both morphologies in relation to coagulant concentration used upon fabrication. All numerical data is reported and labelled as S2 in the supplementary data.

the set dissolved in $[EMIM]^+[Ac]^-$, showing statistical significance for four of the seven samples (samples coagulated in 2%, 5%, 15% and 25% vol. H_2O_2 in H_2O).

As noted above, both sets of samples made from $[EMIM]^+[Ac]^-$ and $[EMIM]^+[Cl]^-$ produced more *overall* amorphous protein secondary structures than crystalline ones in a blended matrix with cellulose. However, there is a discrepancy in sample morphologies when coagulated in identical H_2O_2 solution and dissolved in different IL types. The larger and bulkier Ac^- ion will, for the most part, induce more amorphous structures than the Cl^- ion when the concentration of the coagulant, H_2O_2 solution, is the same. In other words, the smaller Cl^-ion holds the potential to generate more crystalline structures such as β-sheets. One rationale for this discrepancy is that the solvent anion type can effect changes onto protein secondary structure. This is because the smaller Cl^- ion will create less empty space between fibroin chains when interacting with the carbonyl and amide functional groups during dissolution. Furthermore, this effect will allow the protein chains to move into an anti-parallel configuration, forming more β-sheet packing rather than random amorphous structures Schematic 2. depicts an illustration of how the fabrication parameters, $[EMIM]^+[Cl]^-$ and H_2O_2 solution, will change protein morphologies in a matrix blended with cellulose. Furthermore, protein conformation is also known to be dependent upon amino acid sequence, therefore it is interesting to note that the dissolution agent used to solvate protein fibers can influence specific secondary structure conformations.

In future studies, it is important to consider the chemical agents used in our three-step fabrication process, i.e., polymer ratio, solvent anion type, and coagulant type and concentration. For example, water and increasing concentrations of H_2O_2 solution used as a coagulant show only subtle changes to protein structure. However, the solvent anion type in an imidazolium-based IL used to dissolve the polymers influences contrasting protein structure formations within the blended matrix. Therefore, solvent anion type will play a non-trivial role in the dissolution process by affecting the solubility of polymers and thus, altering protein morphology.

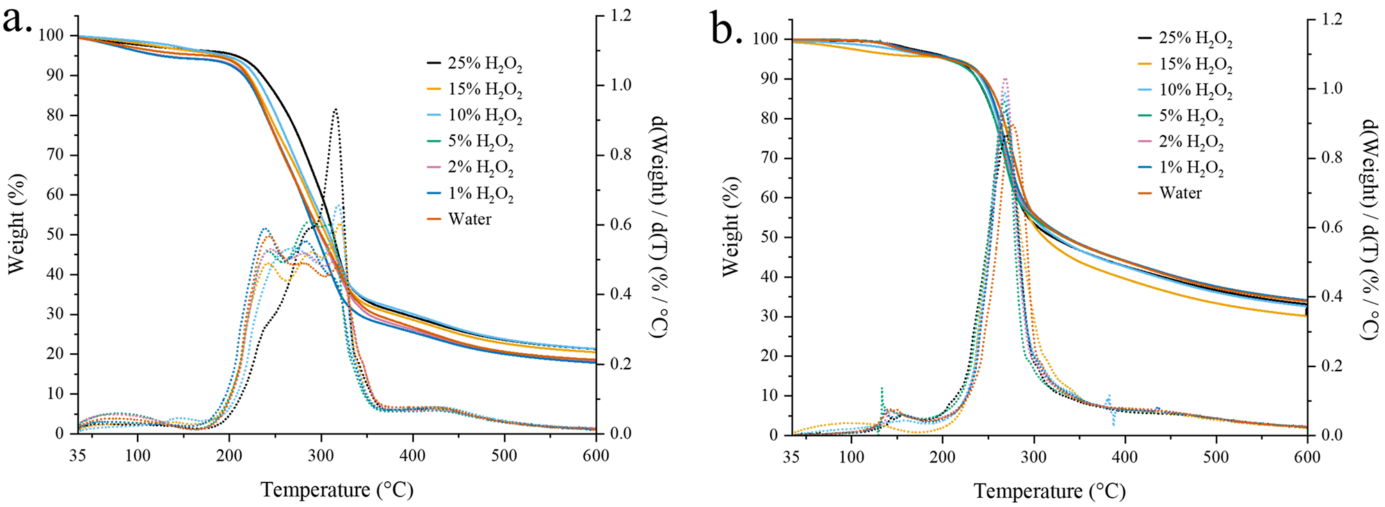

Fig. 4. TGA data showing weight loss% as a function of temperature and its inverse derivative (dotted lines). Plots show regenerated 1:1 CELL-SF composition samples dissolved in IL solvents (a.) $[EMIM]^+[Ac]^-$ and (b.) $[EMIM]^+[Cl]^-$. Samples are differentiated based on the coagulation agents used during regeneration, water and different H_2O_2 solutions (listed on legend).

3.2. Thermogravimetric analysis

Thermogravimetric analysis (TGA) was performed to measure each sample's decomposition temperature at onset, end, and the derivative of percent weight loss with respect to temperature. Total weight loss percent was used to compare overall thermal stability. Refer to Fig. 4 for thermograms of both sample-sets Fig 4a (samples dissolved in [EMIM]$^+$[Ac]$^-$) reveals an interesting trend in the temperature onset of decomposition (TOnset) as a function of increasing H_2O_2 concentrations. Water and lower concentrations of H_2O_2 solution (<5%) show TOnset values ranging between 213.92–219.50 °C, while the TOnset values for samples made with concentrations of H_2O_2 that are 5% and greater show a range between 225.70–265.00 °C. In this case, higher concentrations of H_2O_2 solution used to coagulate blended polymers dissolved in [EMIM]$^+$[Ac]$^-$ will push back the temperature onset of degradation. All thermal analysis values are located in Table 1.

All values for the end temperature of degradation (TEnd) fall within the range of 319.24–335.50 °C and without any noticeable trend for samples dissolved in [EMIM]$^+$[Ac]$^-$. This means that even though the TOnset is correlated to the percent concentration of H_2O_2 used during fabrication, all samples stopped degrading at similar temperatures. Thermograms of this data further reveal that weight loss percentages are between 65.90–69.59%, indicating a similar overall thermal stability among samples dissolved in [EMIM]$^+$[Ac]$^-$. Finally, a trimodal peak, Fig. 4**a**, appears for all but one sample derivative, the 10% H_2O_2-coagulated sample. This sample's plot shows a bimodal derivative with two local peak maxima instead of three. Multimodality within the thermograms' derivative may denote an existence of multiple types of interfaces between crystalline regions of the blend. Two types of interfaces are considered within this work: i. cellulose intercalated with cellulose or likewise SF intercalated with SF and ii. cellulose intercalated with SF. Therefore, parts of the blend would naturally degrade at different rates due to a difference in cohesive energies needed to disrupt intermolecular forces holding the polymer chains together. Morphology of the blend will also induce thermal changes to the system because crystalline regions will degrade slower and at higher temperatures than amorphous regions.

Additionally, another curious trend appears in the thermogram of samples dissolved in [EMIM]$^+$[Ac]$^-$. When examining the derivatives, a greater rate of change in weight loss with respect to temperature occurs at lower temperatures for samples made with water and 1% H_2O_2. While the derivative for the sample coagulated in 2% H_2O_2 shows three similar peak intensities with $d(y)_{1,2,3}$ values where $1 = 0.50,\ 2 = 0.52,$ and $3 = 0.53$. This means that there is a similar rate of change in degradation at three different temperatures upon heating. If we increase the coagulant's concentration to 5% H_2O_2 we begin to see an increase in peak maxima with respect to temperature. For example, the 5% H_2O_2-coagulated sample has values $d(y)_1 = 0.52$ at 242.27 °C, $d(y)_2 = 0.61$ at 287.60 °C, and $d(y)_3 = 0.60$ at 307.77 °C. Therefore, $d(y)_n$ increases in value as temperature rises. This trend becomes even more prominent in the graphs of 10%, 15%, and 25% H_2O_2-coagulated samples, with a noticeable change in $d(y)_{1,2,3}$ values (1 = 0.41, 2 = 0.59, 3 = 0.93) for the sample made from 25% H_2O_2. Therefore, as noted earlier, when we increase in H_2O_2 concentration as the coagulant, we can not only push back the TOnset, but also influence degradation rates. This is because when the sample approaches a certain temperature upon heating, a critical limit is reached where the rate of degradation speeds up. This could also pinpoint changes in the composites' internal morphology which is dependent on H_2O_2 concentration.

These thermal changes are most likely due to a difference in various morphologies induced during the samples' regenerative process. It is reported in previous work (Love et al., 2020) that there exists a *steady* increase in the size of cellulose microcrystals within a blend when using increasing concentrations of H_2O_2 during sample regeneration. Different interface types between microcrystals of various sizes will degrade at different rates because there is a difference in energy needed to disrupt adhesive forces between the chains. Since it is reasonable to expect naturally occurring macromolecules like cellulose and pure silk to have evolved to maximize this adhesive property, polymer chains that are hydrogen-bonded to the same polymer type (cellulose-to-cellulose or silk-to-silk) will have a larger cohesive energy when compared to chains of differing polymer types intermolecularly held together (cellulose--to-silk). This means that more cellulose-to-silk interactions within the interfaces between crystal blocks would result in less thermal stability. In essence, the chains require less energy to separate from one another (Hadadi et al., 2018). With all other things being equal, when two chains of the same polymer type are interacting together at its interfaces, more energy is needed to disrupt the adhesive forces holding the structure together. For this reason, multiple peaks arise in a sample thermogram for the samples dissolved in [EMIM]+[Ac]$^-$. Thermal degradation rate is further related to microcrystalline size (τ), where larger crystals within the system will degrade at higher temperatures and more slowly than smaller crystals and amorphous regions. For example, calculated TΔMax and τ values for samples dissolved in [EMIM]+[Ac]$^-$ and coagulated in 1% H_2O_2 are $d(y_1) = 0.60$ and $\tau = 3.14$ nm, whereas values for the sample coagulated in 25% H_2O_2 within the same set are $d(y_1) = 0.31$ and $\tau = 6.48$. Therefore, a faster relative rate of weight loss with respect to temperature (0.60) was calculated for smaller microcrystals (3.14 nm). This trend is not strictly linear throughout both sets, but the analysis of the calculations does indicate that overall smaller microcrystals will degrade at slower rates with respect to temperature upon heating.

When evaluating the thermal data obtained for the other set (samples dissolved in [EMIM]+[C*l*]$^-$) the TOnset values for samples made with water, 1%, and 2% H_2O_2 are between 248.30–252.78 °C, with water retaining the highest TOnset value. Then, if we increase the concentration of H_2O_2 solution during sample fabrication and test thermal degradation, a drop in TOnset occurs between a small range of 246.77–244.41 °C. Therefore, thermograms of samples made in higher H_2O_2 concentrations show lower TOnset values than those containing the samples coagulated in water and lower concentrations of H_2O_2 solution. This trend differs from the one in the previous set where decomposition temperature is pushed back as a function of increasing coagulant concentrations. Derivatives also differ between the two sets.

Table 1

Thermal analysis data for regenerated 1:1 CELL-SF composition samples dissolved in [EMIM]$^+$[Ac]$^-$ and coagulated in water and different H_2O_2 solutions. Values include the samples' decomposition temperatures at onset (TOnset) and end (TEnd), the percent total weight loss, and the derivative of weight loss with respect to temperature (TΔMax).

[EMIM]$^+$[Ac]$^-$ 1:1 CELL-SF Samples	TOnset (°C)	TEnd (°C)	Weight loss (%)	TΔMax					
				Temp (°C)	$d(y_1)$	Temp (°C)	$d(y_2)$	Temp (°C)	$d(y_3)$
Water	219.5	325.2	68	241.53	0.57	280.86	0.49	318.37	0.48
1% H_2O_2	213.92	319.24	69.59	240.08	0.6	282.83	0.55	312.16	0.45
2% H_2O_2	216.8	334.4	68.1	244.87	0.53	280.95	0.52	216.2	0.5
5% H_2O_2	225.7	327.5	68.6	242.27	0.52	287.6	0.61	307.77	0.6
10% H_2O_2	240.9	333.3	65.9	269.7	0.53	318.38	0.66	–	–
15% H_2O_2	232.1	335.5	67.5	241.68	0.49	288.84	0.52	320.02	0.6
25% H_2O_2	265	330.8	66.7	240.11	0.31	286.85	0.59	315.78	0.93

Within each sample for the set, $[EMIM]^+[Cl]^-$, we see unimodality with only one peak maximum representing a single fastest rate of weight loss with respect to temperature. Interpretation of a unimodal derivative is that more interfaces of a similar polymer type interaction (cellulose-to-cellulose or silk-to-silk) exist within its matrix. Therefore, many similar polymer-type interactions exist within samples dissolved in $[EMIM]^+[Cl]^-$. Refer to Table 2 for all thermal data regarding the $[EMIM]^+[Cl]^-$ set.

Another important and obvious difference between the two sets is the amount of mass lost upon heating (Fig. 4). The samples dissolved in $[EMIM]^+[Cl]^-$ have less total weight loss than the samples within the $[EMIM]^+[Ac]^-$ set. However, when considering samples within their respective sets, there exists a weight loss range of just 4 or 5 percent difference between the water-coagulated sample and the sample made from the highest concentration of H_2O_2. This range difference was calculated for both sets. Therefore, different IL anions (and not coagulate concentrations) affected the *total* thermal stability. Overall thermal stability is greater for samples made from $[EMIM]^+[Cl]^-$ when compared to samples made from $[EMIM]+[Ac]^-$. Refer to Table 1 and Table 2 for all weight loss percentage values.

3.3. *Morphological analysis*

The morphological structure of both sample-sets was analyzed using Wide-angle X-ray Scattering (WAXS). Scattering patterns, as seen in Fig. 5, were acquired between the angle ranges of $2\theta = 15–40^\circ$ and curve fitting was performed to identify and analyze individual peaks. The d-spacing values between lattices were calculated using the Bragg's equation. The main scattering peaks indicating lattice planes (110) and (200) at $2\theta \approx 20.1^\circ$ and 22.0°, respectively, were used to calculate the width sizes of cellulose microcrystals within the blended-polymer samples. Cellulose surface chains within the microcrystal occupy an approximate layer thickness of 0.57 nm (Newman, 1999) and so the proportion of crystallite interior chains was calculated and reported. XRS values may be found in Table 3 for $[EMIM]^+[Ac]^-$ and in Table 4 for $[EMIM]^+[Cl]^-$.

As reported in previously published work (Love et al., 2020) WAXS data presented here confirm both a change from crystalline cellulose I to a semi-crystallized cellulose II as well as a positive correlation between coagulant concentration and microcrystal size. Furthermore, the profiles for samples coagulated in water (both sets) show an amorphous halo represented by a broad peak at $2\theta \approx 20.1^\circ$ A hidden peak at $2\theta \approx 22.0^\circ$ is seen in the halos of samples made from lower concentrations of H_2O_2. (Fig. 5).

A sharp doublet, indicating semi-crystallinity, is clearly seen in the scattering profiles of both sample-sets (Fig. 5). The peak's FWHM is inversely related to crystal size due to the Scherrer equation and thus, smaller values of FWHM indicate larger crystal sizes. When considering the set with samples dissolved in $[EMIM]^+[Ac]^-$, samples regenerated in 10%, 15%, and 25% H_2O_2 solution have FWHM values of decreasing order where 10% has the largest value and 25% has the smallest value. However, for the set of samples dissolved in $[EMIM]^+[Cl]^-$, this doublet begins in the profile for the sample made from 5% H_2O_2 solution. Like the other sample-set, profiles of these samples show an increase in doublet sharpness correlating to increasing concentrations of H_2O_2 solution.

Table 2
Thermal analysis data for regenerated 1:1 CELL-SF composition samples dissolved in $[EMIM]^+[Cl]^-$ and coagulated in water and different H_2O_2 solutions. Values include the samples' decomposition temperatures at onset (TOnset) and end (TEnd), the percent total weight loss, and the derivative of weight loss with respect to temperature (TΔMax).

$[EMIM]^+[Cl]^-$ 1:1 CELL-SF Samples	TOnset (°C)	TEnd (°C)	Weight Loss (%)	TΔMax Temp (°C)	d(y)
Water	252.78	298.03	51.91	276.83	0.9
1% H_2O_2	248.3	291.25	51.86	267.94	0.94
2% H_2O_2	249.15	288.08	51.77	268.48	1.03
5% H_2O_2	244.98	286.05	51.83	267.16	0.96
10% H_2O_2	246.57	290.28	53.41	268.03	0.98
15% H_2O_2	244.41	296.59	56.18	267.56	0.9
25% H_2O_2	246.77	290.35	53.36	268.03	0.98

After calculating the Scherrer equation, values for the samples dissolved in $[EMIM]^+[Ac]^-$ maintain a gradual increase in average crystal size (τ) at lattice plane (110), while the set containing samples dissolved in $[EMIM]^+[Cl]^-$ shows an upwards step-transition of τ between the samples made from 2% and 5% H_2O_2 solution (Fig. 6). For instance, the calculations for the former set, $[EMIM]^+[Ac]^-$, show an increase in τ from 3.13 nm for the 2% H_2O_2-coagulated sample to 3.78 nm for the 5% H_2O_2-coagulated sample. In contrast, calculations for the latter set, $[EMIM]^+[Cl]^-$, show a jump of 2.29 to 5.02 nm in size for 2% and 5% H_2O_2-coagulated samples, respectively. This indicates a change in crystal size transition as a function of solvent anion. Furthermore, when comparing between sets, lower τ values were calculated at lattice plane (110) for samples made from $[EMIM]^+[Ac]^-$ for both the 5% and 10% H_2O_2-coagulated samples. However, once the concentration of H_2O_2 reaches $\geq$15%, τ for both sample-sets were calculated to be between 5.29–6.48 nm in size. Similar results are seen at lattice plane (200), i.e., values calculated for samples dissolved in $[EMIM]^+[Ac]^-$ show a trend with a gradual increase of τ. The other set, $[EMIM]^+[Cl]^-$, possess a step-transition at lattice plane (200) which is similar to values calculated at (110). The difference here is that the samples dissolved in $[EMIM]^+[Cl]^-$ at lattice plane (200) show a more pronounced jump between the 2% and 5% H_2O_2-coagulated samples. However, once the standard error is considered, the probability of this discrepancy decreases between samples. Refer to Fig. 6 for a bar plot showing all values including their SE.

The ratio of crystalline interior chains to its exterior layer (χ) was calculated for both sets and is mathematically dependent upon crystalline size (τ). Therefore, as the values for τ increase, so does χ. χ values calculated at lattice plane (110) are between 0.21–0.68 and between 0.28–0.67 for samples made from $[EMIM]^+[Ac]^-$ and $[EMIM]^+[Cl]^-$, respectively. Furthermore, lower χ values were calculated for the amorphous halos compared to the doublets within the scattering profiles of both sets. At lattice plane (200), values for χ = 0.47–0.73 and 0.29–0.70 for samples dissolved in $[EMIM]^+[Ac]^-$ and $[EMIM]^+[Cl]^-$, respectively. An increased value for χ is calculated for samples regenerated from higher concentrations of H_2O_2. This trend is gradual for the set dissolved in $[EMIM]^+[Ac]^-$ and thus is similar to the trend seen for τ. Samples dissolved in $[EMIM]^+[Cl]^-$ have a positive step-transition for χ values between samples regenerated in 2% and 5% H_2O_2 solutions. These calculations make sense when considering the mathematical relationship of the ratio of crystalline interior chains over its exterior layer to the Scherrer equation. Furthermore, the fabrication's solvent type will produce smaller χ values at lattice plane (200) than at lattice plane (110) when using lower concentrations of H_2O_2 solution (1% and 2% vol. in H_2O) upon regeneration.

Analysis of this data is that there exists distinct differences in cellulose semi-crystallinity as a function of solvent anion type and the concentration of coagulation agent upon fabrication. We theorize that when the negative charge of the solvent's anion interacts with the polymer chains' intermolecular forces during dissolution, effectively disrupting the hydrogen-bonds, the size of the IL anion will correlate to larger or smaller volume spacings between cellulose lattices. Meanwhile, increasing H_2O_2 concentrations during the regenerative phase of the fabrication will induce larger cellulose microcrystals. In these two sample-sets, larger inter-chain spacings are created by the Ac^- ion when compared to the spacing volume created by the smaller Cl^-ion. This larger space permits more H_2O_2 molecules to flow between the polymer chains. Calculated data reveals that the crystal size of cellulose II increases as the concentration of H_2O_2 solution increases during sample regeneration. However, once enough H_2O_2 molecules are introduced

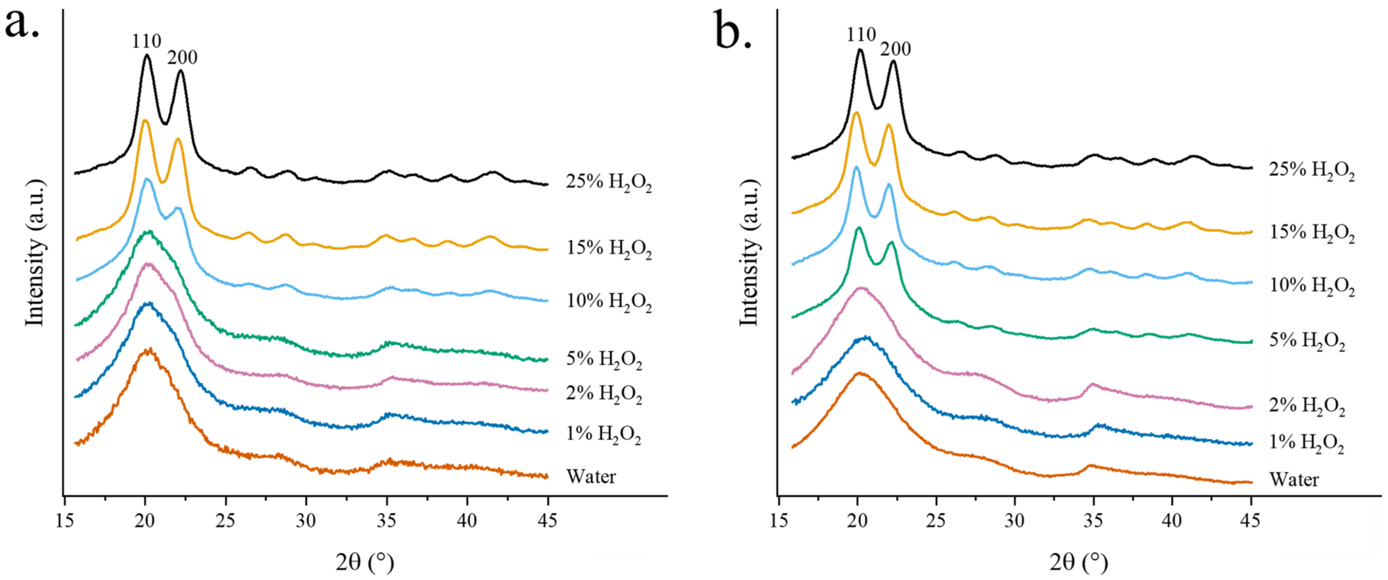

Fig. 5. Normalized wide-angle scattering x-ray data for regenerated 1:1 CELL-SF composition samples dissolved in IL solvents (a.) $[EMIM]^+[Ac]^-$ and (b.) $[EMIM]^+[Cl]^-$. Samples are differentiated based on the coagulation agents and concentrations used during regeneration, water and different H_2O_2 solutions (listed on legend). Peaks representative of lattice planes (110) and (200) are labelled on both plots and were used to measure the mean-width size of cellulose microcrystals at both 2θ angles.

Table 3

Morphological data for regenerated 1:1 CELL-SF composition samples dissolved in $EMIM]^+[Ac]^-$ and coagulated in water and different H_2O_2 solutions. Values include the d-spacing (d) at scattering angle (2θ), mean crystallite size (τ) via the Scherrer equation with its standard error from the mean (SE) $n = 4$, and the proportion of crystallite interior chains (χ). All calculated values were obtained using unnormalized raw XRS data.

$[EMIM]^+[Ac]^-$ 1:1 CELL-SF Sample	lattice plane (110)					lattice plane (200)				
	D (nm)	2θ (°)	mean τ (nm)	±SE $n = 4$	χ	d (nm)	2θ (°)	mean τ (nm)	±SE $n = 4$	χ
Water	0.44	20.27	2.1	< 0.01	0.21	–	–	–	–	–
1% H_2O_2	0.44	20.05	3.14	0.77	0.41	0.41	21.81	3.61	0.46	0.47
2% H_2O_2	0.44	20.11	3.78	0.75	0.49	0.4	21.93	4.28	0.54	0.54
5% H_2O_2	0.44	20.05	3.13	0.86	0.4	0.41	21.81	4.22	1.06	0.53
10% H_2O_2	0.44	20.12	4.18	0.11	0.53	0.4	22.12	6.55	0.33	0.68
15% H_2O_2	0.44	19.99	5.92	0.04	0.65	0.4	22.06	7.32	0.16	0.71
25% H_2O_2	0.44	20.12	6.48	0.03	0.68	0.4	22.19	7.69	0.06	0.73

Table 4

Morphological data for regenerated 1:1 CELL-SF composition samples dissolved in $EMIM]^+[Cl]^-$ and coagulated in water and different H_2O_2 solutions. Values include the d-spacing (d) at scattering angle (2θ), mean crystallite size (τ) via the Scherrer equation with its standard error from the mean (SE), and the proportion of crystallite interior chains (χ). All calculated values were obtained using unnormalized raw XRS data.

$[EMIM]^+[Cl]^-$ 1:1 CELL-SF Sample	lattice plane (110)					lattice plane (200)				
	d (nm)	2θ (°)	mean τ (nm)	±SE $n = 4$	χ	d (nm)	2θ (°)	mean τ (nm)	±SE $n = 4$	χ
Water	0.44	20.06	2.41	0.15	0.28	–	–	–	–	–
1% H_2O_2	0.43	20.47	2.58	0.24	0.31	0.40	22.26	2.48	0.28	0.29
2% H_2O_2	0.44	19.99	2.29	0.12	0.25	0.42	21.22	2.97	1.29	0.38
5% H_2O_2	0.44	20.10	5.02	0.12	0.60	0.40	22.14	6.09	0.40	0.66
10% H_2O_2	0.44	19.93	6.03	0.11	0.66	0.40	21.97	6.97	0.12	0.70
15% H_2O_2	0.45	19.92	5.97	0.04	0.65	0.40	21.97	7.06	0.05	0.70
25% H_2O_2	0.44	20.15	6.36	0.03	0.67	0.40	22.26	6.90	0.08	0.70

into the system, say at 5% or 10% H_2O_2 vol. in H_2O, this volume between chains will become negligible to the formation of semi-crystallinity, producing microcrystal sizes of approximately 4–7 nm at lattice plane (110) and 6–8 nm at lattice plane (200) regardless of solvent anion size.

4. Conclusion

Samples within this study were made from regenerated CELL-SF at a 1:1 polymer blend ratio. Two types of imidazolium-based ionic liquids, $[EMIM]^+[Ac]^-$ verses $[EMIM]^+[Cl]^-$, were used to dissolve the polymers in a comparison-based study. The solvent-polymer substrate was divided up and regenerated in water and six increasing concentrations of H_2O_2 solution (1%, 2%, 5%, 10%, 15%, and 25% vol. in H_2O); there was a total of seven different samples per set. When considering the role of fabrication agents on protein secondary structure, solvent anion type and not coagulant concentration amount influenced changes onto protein morphology. Relative to samples in the $[EMIM]^+[Cl]^-$ set, thermal analysis showed that samples dissolved in $[EMIM]^+[Ac]^-$ are less thermally stable when higher concentrations of H_2O_2 solution is used for fabrication. This trend differs for the samples dissolved in $[EMIM]^+[Cl]^-$ where lower concentrations of H_2O_2 solution show more thermostability. Thermograms show derivatives of multimodality for

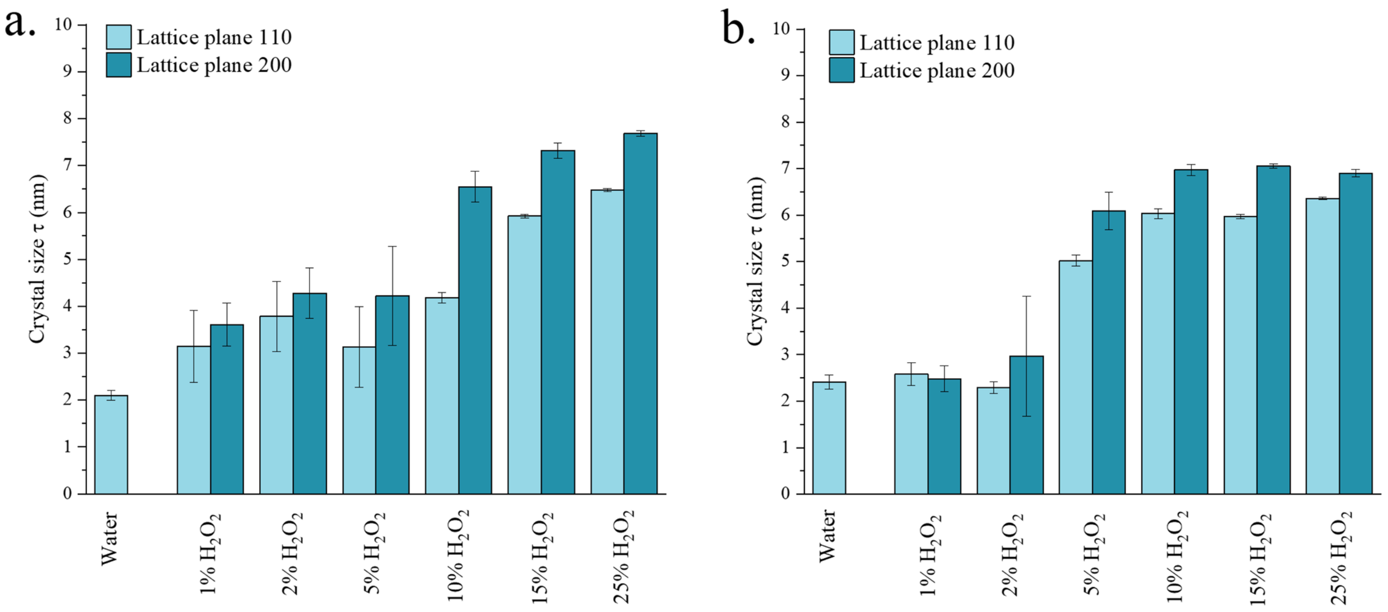

Fig. 6. For visualization purposes, bar graphs are reported for carbohydrate microcrystal width size values (τ) at lattice planes (110) and (200) for regenerated 1:1 CELL-SF composition samples dissolved in IL solvents (a.) $[EMIM]^+[Ac]^-$ and (b.) $[EMIM]^+[Cl]^-$. Samples are differentiated based on the coagulation agents used during regeneration, water and different H_2O_2 solutions (listed on x-axis).

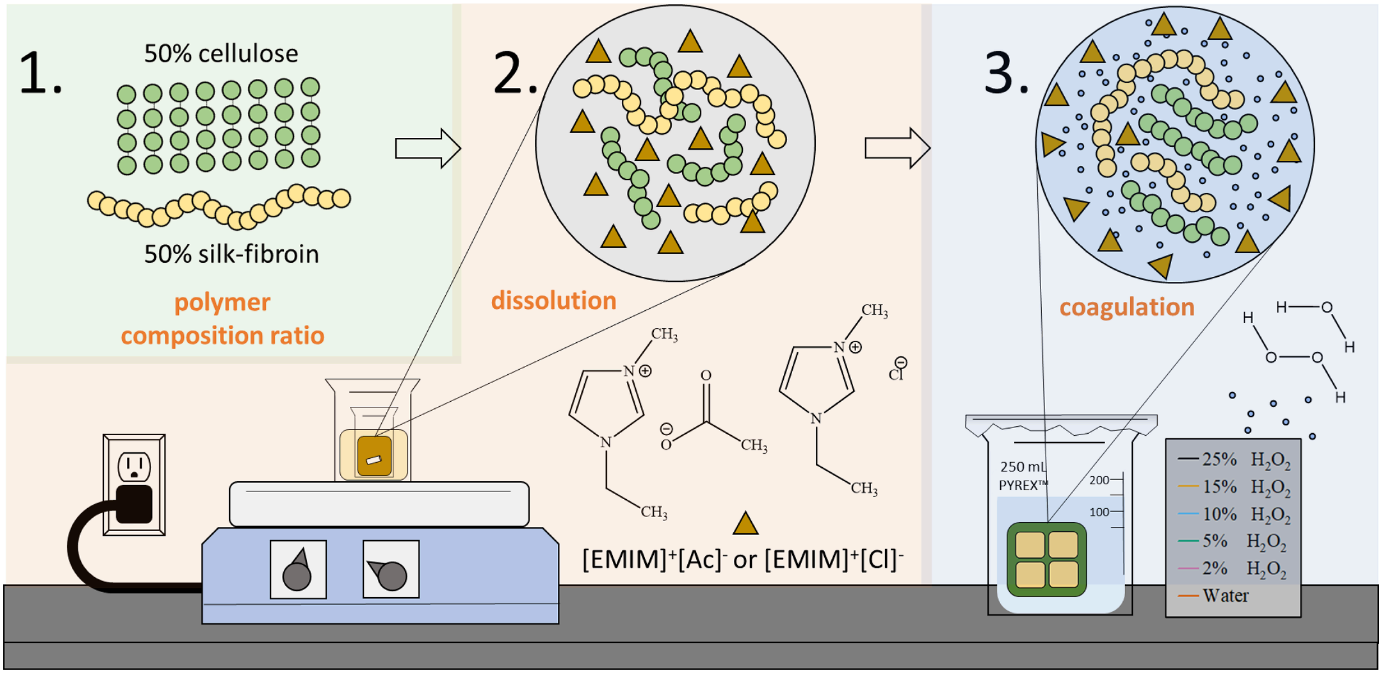

Schematic 1. This image shows a three-step fabrication process to regenerate a 1:1 blended polymer. *Step 1* illustrates a polymer composition ratio of 1:1 cellulose (green) to silk-fibroin (yellow) with 10% polymer content to 90% solvent content. *Step 2* is the polymer dissolution phase with solvents, $[EMIM]^+[Ac]^-$ or $[EMIM]^+[Cl]^-$ (brown triangles). *Step 3* is the polymer coagulation phase where the polymer-solvent material is placed in a PDMS mold and submerged in a closed container of 100 mL solution, D.I. water or H_2O_2 solutions (small blue circles). The product is then removed from its bath and dried in a vacuum oven set to 30 inHg at 50 °C for 24 h.

$[EMIM]^+[Ac]^-$ and unimodality for $[EMIM]^+[Cl]^-$. Within each respective set, similar total weight loss percentages were calculated, but over-all thermostability of the $[EMIM]^+[Cl]^-$ set was greater than the $[EMIM]^+[Ac]^-$ set. During fabrication of the blended samples, microcrystalline cellulose converted from cellulose I to a semi-crystallization state of cellulose II. Intensity of these peaks is positively correlated to increasing amounts of H_2O_2 concentration and begin to appear in the profiles of the 10% H_2O_2-coagulated sample in the $[EMIM]^+[Ac]^-$ set and the 5% H_2O_2-coagulated sample in the $[EMIM]^+[Cl]^-$ set. Cellulose crystal sizes were positively correlated to H_2O_2 concentration and were calculated to have a gradual increase in size for the $[EMIM]^+[Ac]^-$ set verses a positive step transition for the $[EMIM]^+[Cl]^-$ set. Lower values for the proportion of crystallite interior chains were calculated for amorphous halos compared to doublets within the scattering profiles of both sets. Overall, analysis of this data is that there exists a means to fine-tune specific semi-crystalline properties of both cellulose and SF by

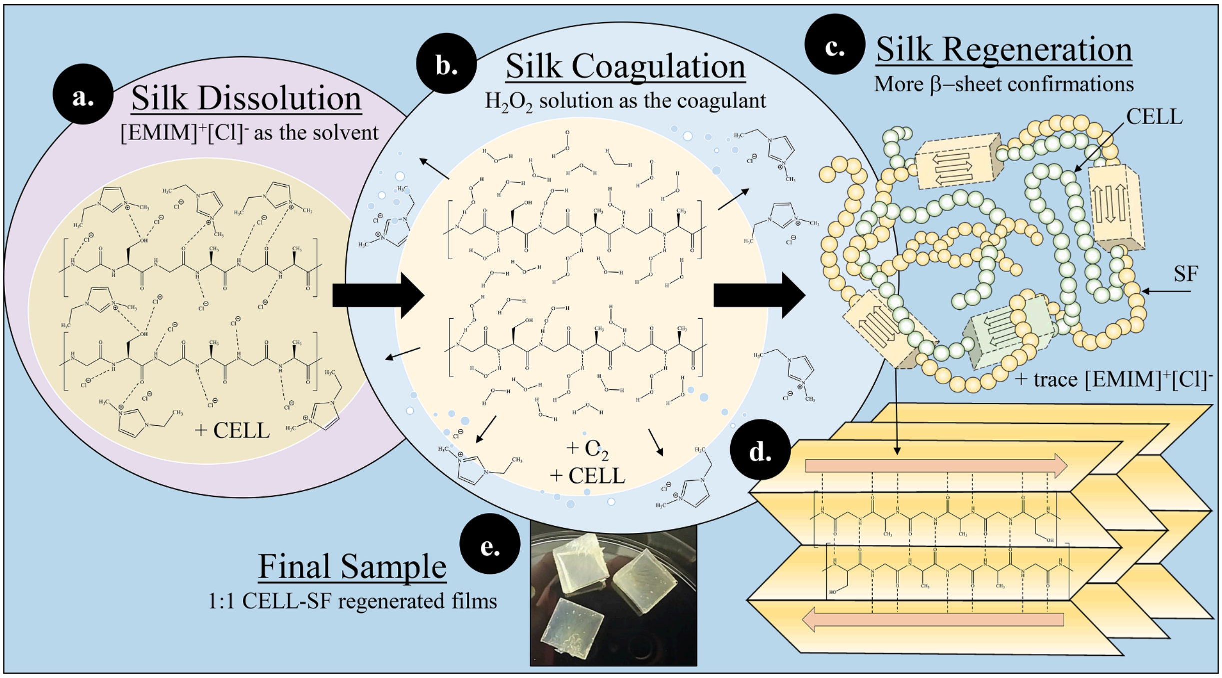

Schematic 2. Illustration showing the influence of fabrication parameter $[EMIM]^+[Cl]^-$ as the solvent on SF secondary structure in a 1:1 CELL-SF composition sample: (a.) hydrogen-bond disruption between SF chains by $[EMIM]^+[Cl]^-$ under heat and agitation; (b.) coagulation of SF chains and solvent diffusion by water and H_2O_2 molecules in situ; (c.) intercalation of regenerated cellulose and SF in a blended polymer sample after 48 hr. of coagulation; (d.) cartoon of a SF β-sheet conformation, and (e.) final product of regenerated samples.

changing the concentration of the coagulant, H_2O_2 solution, and the solvent anion type, respectively. Therefore, when utilizing the three-step fabrication process reported in this work, it is important to consider the chemical agents used in the production of a blended-polymer system.

Declaration of Competing Interest

This article and its content has not been published previously by any of the authors, nor is it under consideration for publication in another journal at this time. All authors have seen and approved the revised manuscript for submission.

Acknowledgments

The authors are grateful for financial support from NSF-DMR-RUI (1809354 and 1809541), Rutgers-Camden Arts and Sciences Start-up Package, State of NJ ELF Grant and The Center for Computational and Integrative Biology TA Funds. DEXS System is supported by NSF-MRSEC (17–20530), NSF-MRI (17–25969), ARO DURIP (W911NF-17–1–02822), and the University of Pennsylvania. A special thank you to Dr. Paul Heiney, Department of Physics and Astronomy at the University of Pennsylvania for technical support and training on the DEXS system. Salas-de la Cruz summer financial support was provided by NSF-CMMI (2037097) and NSF-DMR (2104376).

Supplementary materials

Supplementary material associated with this article can be found, in the online version, at doi:10.1016/j.carpta.2022.100193.

References

Achour, S., Hamada, B., Baroudi, S., Abdelaziz, A., Rezazgui, I., & Trache, D. J. J.o. M. L. (2021). Spectroscopic characterization andthermal decomposition kinetics of 1, 3-dibutyl-imidazolium bromide synthesized through a solvent-free and one-pot method. *Journal of Molecular Liquids, 339*, Article 117266.

Bealer, E. J., Onissema-Karimu, S., Rivera-Galletti, A., Francis, M., Wilkowski, J., Salas-de la Cruz, D., et al. (2020). Protein–polysaccharide composite materials: Fabrication and applications. *Polymers, 12*(2), 464.

Benedetto, A., Ballone, P. J. A. S. C., & Engineering. (2016). Room temperature ionic liquids meet biomolecules: A microscopic view of structure and dynamics. *ACS Sustainable Chemistry & Engineering, 4*(2), 392–412.

Blessing, B., Trout, C., Morales, A., Rybacki, K., Love, S. A., Lamoureux, G., et al. (2020). The impact of composition and morphology on ionic conductivity of silk/cellulose bio-composites fabricated from ionic liquid and varying percentages of coagulation agents. *Polymer International, 21*(13), 4695.

Blessing, B., Trout, C., Morales, A., Rybacki, K., Love, S. A., Lamoureux, G., et al. (2019). Morphology and ionic conductivity relationship in silk/cellulose biocomposites. *International journal of molecular sciences, 68*(9), 1580–1590.

DeFrates, K., Markiewicz, T., Callaway, K., Xue, Y., Stanton, J., Salas-de la Cruz, D., et al. (2017). Structure–property relationships of Thai silk–microcrystalline cellulose biocomposite materials fabricated from ionic liquid. *International journal of biological macromolecules, 104*, 919–928.

French, A. D., & Cintrón, M. S. J. C. (2013). Cellulose polymorphy, crystallite size, and the segal crystallinity index. *Cellulose (London, England), 20*(1), 583–588.

Gough, C. R., Rivera-Galletti, A., Cowan, D. A., Salas-De La Cruz, D., & Hu, X. J. M. (2020). Protein and polysaccharide-based fiber materials generated from ionic liquids: A review. *Molecules (Basel, Switzerland), 25*(15), 3362.

Hadadi, A., Whittaker, J. W., Verrill, D. E., Hu, X., Larini, L., & Salas-De La Cruz, D. J. B. (2018). A hierarchical model to understand the processing of polysaccharides/protein-based films in ionic liquids. *Biomacromolecules, 19*(10), 3970–3982.

Hu, X., Kaplan, D., & Cebe, P. J. M. (2006). Determining beta-sheet crystallinity in fibrous proteins by thermal analysis and infrared spectroscopy. *Macromolecules, 39*(18), 6161–6170.

Isogai, A., & Atalla, R. J. C. (1998). Dissolution of cellulose in aqueous NaOH solutions. *Cellulose (London, England), 5*(4), 309–319.

Kovalenko, V. I. J. R. C. R. (2010). Crystalline cellulose: Structure and hydrogen bonds. *Russian Chemical Reviews, 79*(3), 231.

Liu, Z., Wang, H., Li, Z., Lu, X., Zhang, X., & Zhang, S. (2011). Physics characterization of the regenerated cellulose films in ionic liquids and rheological properties of the solutions. *Materials Chemistry and Physics, 128*(1–2), 220–227.

Love, S. A., Popov, E., Rybacki, K., Hu, X., & Salas-de la Cruz, D. J. I. J.o. B. M. (2020). Facile treatment to fine-tune cellulose crystals in cellulose-silk biocomposites through hydrogen peroxide. *International journal of biological macromolecules, 147*, 569–575.

Marsh, K. N., Boxall, J. A., & Lichtenthaler, R. J. F.p.e (2004). Room temperature ionic liquids and their mixtures—A review. *Fluid phase equilibria, 219*(1), 93–98.

Rose J. Miller, Vanessa M. Smith, Stacy A. Love, Sarah M. Byron, David Salas-de la Cruz, and Kevin M. Miller, ACS Applied Polymer Materials 2021 3 (2), 1097-1106 DOI: 10.1021/acsapm.0c01327.

Newman, R. H. J. S.s.n.m.r (1999). Estimation of the lateral dimensions of cellulose crystallites using 13C NMR signal strengths. *Solid state nuclear magnetic resonance, 15*(1), 21–29.

Nishino, T., Takano, K., & Nakamae, K. J. J.o. P. S. P. B. P. P. (1995). Elastic modulus of the crystalline regions of cellulose polymorphs. *Journal of Polymer Science Part B: Polymer Physics, 33*(11), 1647–1651.

Noorhisham, N. A., Amri, D., Mohamed, A. H., Yahaya, N., Ahmad, N. M., Mohamad, S., et al. (2021). Characterisation techniques for analysis of imidazolium-based ionic liquids and application in polymer preparation: A review. *Journal of Molecular Liquids*, Article 115340.

Oldenkamp, H. F., Vela Ramirez, J. E., & Peppas, N. A. J. R.b. (2019). *Re*-evaluating the importance of carbohydrates as regenerative biomaterials. *Regenerative biomaterials, 6*(1), 1–12.

Phillips, D. M., Drummy, L. F., Conrady, D. G., Fox, D. M., Naik, R. R., Stone, M. O., et al. (2004). Dissolution and regeneration of Bombyx mori silk fibroin using ionic liquids. *Journal of the American chemical society, 126*(44), 14350–14351.

Poletto, M., Zattera, A. J., Forte, M. M., & Santana, R. M. J. B. T. (2012). Thermal decomposition of wood: Influence of wood components and cellulose crystallite size. *Bioresource Technology, 109*, 148–153.

Qi, Y., Wang, H., Wei, K., Yang, Y., Zheng, R.-. Y., Kim, I. S., et al. (2017). A review of structure construction of silk fibroin biomaterials from single structures to multi-level structures. *International Journal of Molecular Sciences, 18*(3), 237.

Stanton, J., Xue, Y., Pandher, P., Malek, L., Brown, T., Hu, X., et al. (2018). Impact of ionic liquid type on the structure, morphology and properties of silk-cellulose biocomposite materials. *International Journal of Biological Macromolecules, 108*, 333–341.

Šturcová, A., Davies, G. R., & Eichhorn, S. J. J. B. (2005). Elastic modulus and stress-transfer properties of tunicate cellulose whiskers. *Biomacromolecules, 6*(2), 1055–1061.

Tarchoun, A. F., Trache, D., Klapötke, T. M., & Khimeche, K. J. C. E. J. (2020a). Tetrazole-functionalized microcrystalline cellulose: A promising biopolymer for advanced energetic materials. *Chemical Engineering Journal, 400*, Article 125960.

Tarchoun, A. F., Trache, D., Klapötke, T. M., Krumm, B., Khimeche, K., & Mezroua, A. J. C. P. (2020b). A promising energetic biopolymer based on azide-functionalized microcrystalline cellulose: Synthesis and characterization. *Carbohydrate Polymers, 249*, Article 116820.

Valluzzi, R., Gido, S. P., Muller, W., & Kaplan, D. L. J. I.j.o.b.m. (1999). Orientation of silk III at the air-water interface. *International journal of biological macromolecules, 24*(2–3), 237–242.

Wada, M. J. M. (2001). In situ observation of the crystalline transformation from cellulose IIII to Iβ. *Macromolecules, 34*(10), 3271–3275.

Wang, Q., Chen, Q., Yang, Y., & Shao, Z. J. B. (2013). Effect of various dissolution systems on the molecular weight of regenerated silk fibroin. *Biomacromolecules, 14*(1), 285–289.

Yao, Y., Zhang, E., Xia, X., Yu, J., Wu, K., Zhang, Y., et al. (2015). Morphology and properties of cellulose/silk fibroin blend fiber prepared with 1-butyl-3-methylimidazolium chloride as solvent. *Cellulose (London, England), 22*(1), 625–635.

Yue, Yiying, (2011). A comparative study of cellulose I and II and fibers and nanocrystals . LSU Master's Theses. 764. https://digitalcommons.lsu.edu/gradschool_theses/764 Identifier: etd-06062011-143639.

Zhu, S., Wu, Y., Chen, Q., Yu, Z., Wang, C., Jin, S., et al. (2006). Dissolution of cellulose with ionic liquids and its application: A mini-review. *Green Chemistry, 8*(4), 325–327.